Bone Reports 9 (2018) 122–131

Contents lists available at ScienceDirect

Bone Reports

journal homepage: www.elsevier.com/locate/bonr

Ptychographic X-ray CT characterization of the osteocyte lacuno-canalicular network in a male rat's glucocorticoid induced osteoporosis model

Antonia Ciani[a,b], Hechmi Toumi[b,c,1], Stéphane Pallu[b,1,2], Esther H.R. Tsai[d], Ana Diaz[d], Manuel Guizar-Sicairos[d], Mirko Holler[d], Eric Lespessailles[b,c], Cameron M. Kewish[a,*,3]

[a] Synchrotron Soleil, L'Orme des Merisiers, 91192 Gif-sur-Yvette, France
[b] EA4708, Imagerie Multimodale, Multiéchelles et Modélisation du Tissu Osseux et Articulaire (I3MTO), Université d'Orléans, 45000 Orléans, France
[c] Département Rhumatologie, Centre Hospitalier Régional d'Orléans, 45067 Orléans, France
[d] Paul Scherrer Institut, 5232 Villigen, Switzerland

ARTICLE INFO

Keywords:
Osteocytes
Glucocorticoid-induced osteoporosis
Nano-CT
Quantitative analysis
Ptychography

ABSTRACT

Ptychographic X-ray computed tomography (PXCT) is a quantitative imaging modality that non-destructively maps the 3D electron density inside an object with tens of nanometers spatial resolution. This method provides unique access to the morphology and structure of the osteocyte lacuno-canalicular network (LCN) and nanoscale density of the tissue in the vicinity of an osteocyte lacuna. Herein, we applied PXCT to characterize the lacunae and LCN in a male Wistar rat model of glucocorticoid-induced osteoporosis (GIO). The ptychographic images revealed significant ($p < 0.05$) differences in the number of canaliculi originating from the lacuna per ellipsoidal surface unit, Ca.Nb ($p = 0.0106$), and the 3D morphology of the lacuna ($p = 0.0064$), between GIO and SHAM groups. Moreover, the mean canalicular diameter, Ca.Dm, was slightly statistically un-significantly smaller in GIO (152 ± 6.5) nm than in SHAM group (165 ± 8) nm ($p = 0.053$). Our findings indicate that PXCT can non-destructively provide detailed, nanoscale information on the 3D organization of the LCN in correlative studies of pathologies, such as osteoporosis, leading to improved diagnosis and therapy.

1. Introduction

Bone is a dynamic "organic-inorganic" tissue able to adapt to environmental and temporal changes through remodeling processes performed by osteoclasts, osteoblasts and osteocytes (Henkel et al., 2013). Osteocytes are the last differentiated state of the "osteoblast-osteocyte" lineage. They are the most long-lived cells in the skeleton, embedded within an extensive and intricate network of cavities and channels in the bone matrix, called *lacunae* and *canaliculi*, respectively (Bonewald, 2011). Thanks to their interconnectivity, osteocytes can communicate and exchange nutrients and waste products (Fritton and Weinbaum, 2009). The movements of extracellular fluids within the *lacuno-canalicular* network (LCN) mediate external stimuli to the osteocytes, implicating the architecture of this network in mechano-transduction pathways and bone remodeling. The morphology of the lacunae housing the osteocytes has been shown to depend on the osteoarticular physiopathological context, varying, *e.g.*, in osteoarthritis, osteoporotic bone, and osteopetrotic osteocytes (van Hove et al., 2009; Schneider et al., 2010; Schneider et al., 2011). The lifecycle and health of individual osteocytes affects the state of the LCN within bone tissue (Dallas and Veno, 2012). Hence, the functional cellular syncytium and the common fluid space defined by the LCN are interrelated, and depend on the viability of the osteocytes and the health of the bone tissue (You et al., 2004). Osteocytes change in size and shape as they lose viability, and the bone remodeling cycle may be initiated to remove non-viable cells. Lacunae previously occupied by healthy cells may remain empty, or become mineralized and occluded (Frost, 1960; Currey, 1964).

Consequently, a three-dimensional (3D) characterization of the LCN is necessary to improve our understanding of bone functionality and

* Corresponding author.
E-mail address: cameron.kewish@synchrotron.org.au (C.M. Kewish).
[1] Both of these authors contributed equally to this work.
[2] Current address: UMR CNRS 7052 CNRS Laboratoire de Bioingénierie et Bioimagerie Ostéoarticulaire (B2OA), UFR de Médecine, Université Paris Diderot, 75010 Paris, France.
[3] Current address: ARC Centre of Excellence in Advanced Molecular Imaging, La Trobe University, Bundoora VIC 3086, Australia; and Australian National Science and Technology Organisation, Australian Synchrotron, Clayton VIC 3168, Australia.

https://doi.org/10.1016/j.bonr.2018.07.005
Received 21 May 2018; Accepted 27 July 2018
Available online 29 July 2018

bone diseases. The key outcome of this study was a comprehensive, non-destructive and quantitative characterization of the LCN in high 3D resolution *via* ptychographic X-ray computed tomography (PXCT), allowing us to examine in detail the physiological impact of glucocorticoid-induced osteoporosis (GIO) at the sub-cellular level in cortical bone. We characterized the LCN in the presence of GIO in male rats and made a comparison with healthy paired-age rats.

Glucocorticoid (GC) therapy is used extensively, especially in chronic inflammatory and autoimmune diseases. Patients receiving long-term GC treatment present fractures in 30–50% of cases (Briot and Roux, 2015). Osteoporosis is one of the most widespread diseases in the world, resulting in bone fragility and enhancing the risk of fracture, and GIO is the most frequent cause of secondary osteoporosis (van Staa, 2006). In GIO, bone fragility occurs before changes in bone mineral density (BMD) are detectable, and the increases in fracture risk are larger than those expected on the basis of BMD changes (Van Staa et al., 2003; Weinstein, 2010; Van Staa et al., 2002). Fractures induced by GC therapy could, therefore, result from other factors than a decrease in BMD. The pathophysiology of GIO has not yet been completely explained (Frenkel et al., 2015). Among other mechanisms GC interferes with the adipocytic pathway but also with Wnt signalling pathway notably the upregulation of its inhibitor Dickkopf-1 (Ohnaka et al., 2004). At the cellular level, GC excess has adverse effects on bone cells (Weinstein, 2000; Weinstein, 2011; Weinstein et al., 2002), causing osteoblast (Weinstein, 2000) and osteocyte apoptosis (Weinstein et al., 1998; Jia et al., 2006; O'Brien et al., 2004; Sambrook et al., 2003; Achiou et al., 2015). Experiments strongly suggest that GC excess adversely affects bone vasculature due to direct effects on osteocytes (Weinstein et al., 2010).

Glucocorticoid-induced osteocyte apoptosis (Achiou et al., 2015) and decreasing bone vasculature could be implicated in a loss of bone strength before changes in BMD occur (Weinstein et al., 2010; Canalis et al., 2007). This could account for the observed mismatch between BMD and fracture risk in patients with GIO (Van Staa et al., 2003; Van Staa et al., 2005; Kanis et al., 2004).

The motivation for this study is to build upon these previous results, investigating GC induced modifications of the LCN structure at the nanoscale, to give new insights into how this network is modified in conditions of high rates of osteocyte apoptosis, and the correlation between mineral matrix and organic tissue. A thorough understanding of the nanoscale structure of cortical bone could shed light on the effects of GC treatment at the sub-cellular level and if so, provide the means to design effective co-administered therapies.

X-ray imaging exploits short wavelength radiation to produce images with high density contrast and high spatial resolution, simultaneously separating bone from soft tissue, and revealing the nanostructure of each component. Ultramicroscopy using X-ray optics has been achieved fairly recently (Langer and Peyrin, 2016; Schroer et al., 2002). Coherent 3D X-ray imaging has been demonstrated for the particular case of ultra-microscopy on bone using ptychographic X-ray computed tomography (PXCT) (Dierolf et al., 2010) and holography (Langer et al., 2012). Other options for performing ultramicroscopic imaging of bone tissue in 3D are transmission electron microscopy (Rubin et al., 2003; Everts et al., 2012), serial sectioning focused-ion beam scanning electron microscopy (Schneider et al., 2011), and confocal laser scanning microscopy (Jones et al., 2005). Compared to X-ray microscopy these methods obtain information from very thin specimens, or regions of a sample that are close to the surface, and both the sample preparation and the imaging are destructive in nature.

PXCT is a scanning coherent X-ray diffraction microscopy technique in which high-resolution images of a sample are obtained from diffraction data with iterative phase retrieval algorithms. Information from scanning a sample in a coherent beam such that illuminated areas overlap is used to aid the recovery of the unmeasurable phases that are associated to the far field diffraction intensities (Faulkner and Rodenburg, 2004; Thibault et al., 2008). Fig. 1 shows a schematic illustration of the experimental geometry for PXCT image acquisition.

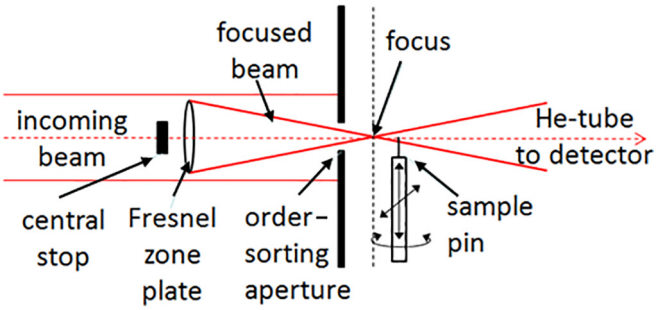

Fig. 1. A schematic illustration of the experimental geometry for ptychographic data acquisition. The beam is focused by a Fresnel zone plate, increasing the flux density on the sample, which is supported on a scanning and rotation stage. The diffraction signal is measured by a detector in the far field (not shown).

Complex-valued maps of the transmission function retrieved in this way represent the projection of the X-ray absorption and refraction properties of the sample. Different projections are achieved by rotating the sample around an axis perpendicular to the beam. Quantitative 3D images of the electron density within objects are obtained using CT algorithms, such as filtered backprojection (FBP) to invert the phase component of the projection images (Dierolf et al., 2010).

Cortical bone samples from the tibial diaphysis of rat bones were analyzed through a quantitative method we have developed, previously reported by Ciani et al. (2016) which provides a microarchitectural characterization of the LCN in terms of a morphological description of the osteocyte lacunae and a geometrical description of the canaliculi. Fig. 2 shows a sketched cross-section of an osteocyte lacuna and canaliculi as a guide to the following discussion.

Lacuna morphology was analyzed in terms of shape, volume, and degree of anisotropy. At the canalicular level, the porosity, spatial density of the network connections to the lacuna surface, and the mean canalicular radius was computed. The LCN structure of GIO samples were compared with the microarchitecture in healthy (SHAM) samples. To our knowledge, this is the first time that the effects of GC treatment on the LCN in a GIO rat experimental model have been studied at this scale of spatial resolution in 3D.

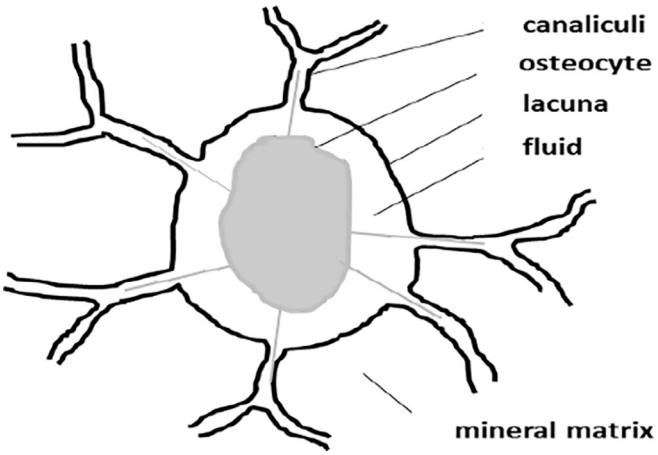

Fig. 2. A sketch of an osteocyte section with its lacuna and canaliculi and surrounding matrix. The osteocyte (cell body + cytoplasmic processes) is represented in gray. The lacuna, or the cavity in which the cells are located, and the canaliculi are outlined in black.

Table 1
Summary of the experiment parameters for the three imaging experiments. The photon energy was 6.2 keV in all cases; the beam defining optic was either a 3 μm-diameter pinhole aperture or a Fresnel zone plate (FZP). The reconstructed voxel size $d_{voxel} = \lambda D/nd_{pixel}$ is determined from the experiment geometry and the region of interest (ROI) is extracted from each far-field diffraction pattern. The field of view (FOV) in the reconstructed images depends on the scanned area.

Experiment	Beam defining optics	Beam size on sample [μm]	Detector distance, D [m]/pixel size, d_{pixel} [μm]	Number of projections, N_{proj}	Acquisition time [h]	ROI size n × n [pixels^2]	Voxel side length, d_{voxel} [nm]	Average FOV [μm]
1	Pinhole	3	7.198 m 172 μm	240	13	192 × 192	43.6	50 × 30
2	FZP	5.6	7.331 m 172 μm	240	14	192 × 192	44.4	75 × 30
3	FZP	9	7.342 m 75 μm	350–800	11	500 × 500/450 × 450	39.1/43.3	80 × 40

2. Material and methods

2.1. Animal samples

The animal sample preparation protocol was previously described by Achiou et al. (2015). To briefly summarize: male Wistar rats, 17 weeks-old at the beginning of the experiment, were purchased from Janvier Animal Production (Genest Saint-Isle, France). Animals were maintained in a controlled environment with temperature 22 ± 3 °C and under 12 h/12 h light-dark cycles for the duration of the experiment. The rats were housed two per standard cage with *ad libitum* access to water and commercial standard diet (M20, SDS, France). Food intake was recorded weekly for all groups. After acclimation, at 19 weeks of age, the rats were randomly assigned to a control group (SHAM) or a methylprednisolone-treated group (GIO). Methylprednisolone (Sigma, France) was injected subcutaneously at 5 mg/kg, 5 times per week (Achiou et al., 2015). The control rats were subcutaneously injected with vehicle (saline) twice a week. The protocol lasted 9 weeks. The study was approved by a board institution and an ethics committee (Agreement n° C45-234-9 and 2011-11-2) from the French Institute INSERM (Institut National de la Santé et de la Recherche Médicale) and from the agriculture council (Ministère de l'Agriculture, France, approval ID: INSERM45-001). Diaphyseal bone sections were obtained and fixed in formalin 4% v/v at 4 °C. Transverse sections from upper half of the tibial diaphysis, approximately 1 cm-diameter, were sliced using a rotary diamond saw (Dremel 300) to between 150 and 250 μm-thickness. From these sections, sample pieces of about 50 × 50 × 50 μm^3 (verified by transmission visible-light microscopy to contain at least one osteocyte lacuna) were resected and glued onto the points of needles fixed on suitable holders for ptychographic X-ray CT image acquisition. A total of 11 such free-standing bone specimens were analyzed by this method; 6 samples from the GIO group belonging to 4 different rats, and 5 samples from the SHAM group, belonging to 5 different rats.

2.2. Morphological and topological characteristics of the trabecular bone

The trabecular microarchitecture of the distal metaphysis of the left femurs from Achiou et al. (2015)'s study was evaluated *post mortem* using μCT (Skyscan 1072; Skyscan, Kontich, Belgium) (n = 14 samples for the SHAM group, n = 15 samples for the GIO group). The X-ray source was set at 85 kV and 100 μA, and 400 projections were acquired over an angular range of 180° (angular step of 0.45°). Images were reconstructed to an isotropic pixel size of 11.16 μm and 225 slices were selected from the distal femur metaphysis for analysis from each sample. The trabecular region of interest (ROI) was drawn manually and the following parameters were measured using the Skyscan μCT Analyzer software: bone volume/tissue volume (BV/TV) and trabecular thickness (Tb.Th).

2.3. Morphological characteristics of cortical bone

For analysis of cortical bone, we used the reconstructed 2D bone slices obtained by micro-CT of the previous left femur at mid-diaphysis (n = 14 samples for the SHAM group, n = 15 samples for the GIO group). The 225 slice images of each sample were analyzed using algorithms previously developed; briefly, cortical bone was separated from trabecular bone, and then converted to a binary image using a threshold adapted to each sample to determine cortical bone area. We used the same acquisition characteristics as for trabecular bone. After reconstruction, the cortical bone was extracted by drawing polygonal contour with CT analyzer software. Before inversion of the threshold, we applied simple global thresholding methods, and the algorithms developed for trabecular bone analysis were used to determine the cortical bone area (Ct.Ar).

2.4. Cortical bone section preparation, toluidine blue staining

Bone tibia slices (thickness below 400 μm) from the two groups (SHAM, n = 7; GIO, n = 7) from Achiou et al. (2015)'s study were cut transversally in the superior half of the tibia diaphysis with a high-speed rotary tool (Dremel 300). Fixation, embedding in Epoxy resin, toluidine blue staining, light microscopy ImageJ (Schneider et al., 2012) analysis was done as previously shown (Achiou et al., 2015). The percentage of osteocyte lacunar occupancy and osteocyte lacunae area was calculated.

2.5. Ptychographic X-ray CT image acquisition

The samples were imaged at the cSAXS beamline of the Swiss Light Source at the Paul Scherrer Institut in Villigen, Switzerland, in three different rounds of experiments. The X-ray photon energy, E, was 6.2 keV in all cases. Due to the evolution of the imaging apparatus at the cSAXS beamline, three different versions of a PXCT scanning instrument were used (see Table 1). The first experiment used an apparatus identical to that reported by Dierolf et al. (2010), recording diffraction data with a PILATUS 2M detector having pixel size d_{pixel} = 172 μm (Kraft et al., 2009). The second experiment utilized used a high-stability environment (Holler et al., 2012; Holler et al., 2014), which employed interferometric measurement of the position and stability of the sample during data acquisition (Holler and Raabe, 2015) and further facilitated automated loading of samples and scan volume alignment. The third experiment used the latter system with an EIGER detector (Johnson et al., 2012), enabling more projections to be recorded for each PXCT dataset. We note that although the experiment conditions varied, we ensured that the beam energy and sample-to-detector geometry, which define the reconstructed object pixel size in ptychographic imaging, were almost constant and the quantitative nature of PXCT (Diaz et al., 2012) allows us to directly compare the results in all cases.

The total X-ray dose imparted to the specimens can be estimated

from the incident flux density (Howells et al., 2009), which was different when using the pinhole (experiment 1) and the Fresnel zone plate (FZP) (experiments 2 and 3) to define the beam on the sample. Assuming a bone composition of pure hydroxyapatite [$Ca_{10}(PO_4)_6(OH)_2$] with density 2 g/cm^3, and X-ray flux densities of 2.3×10^5 photons/μm^2 for the pinhole and 1.3×10^7 photons/μm^2 when using the FZP, we estimate that doses of the order of 10^6 Gy and 5.6×10^7 Gy, respectively, were imparted to the bone specimens during PXCT scanning (Ciani et al., 2016). At these X-ray doses, it would only be feasible to image organic tissue intact with cryogenic protection against radiation damage (Howells et al., 2009). Nevertheless, the measured data allow for a full analysis of the mineral matrix in which the lacunae and their dendritic processes were found. Ptychographic reconstructions were obtained using the difference map algorithm (Thibault et al., 2008; Thibault et al., 2009), with maximum-likelihood refinement (Thibault and Guizar-Sicairos, 2012). The region of interest (ROI) in reciprocal space extracted from each diffraction pattern is listed as n × n pixels^2 in Table 1 which, with detector distance D and the photon wavelength λ, defines the isotropic reconstructed voxel side-length $d_{voxel} = \lambda D / nd_{pixel}$. The reconstructed complex-valued images represent the transmissivity of the sample (Faulkner and Rodenburg, 2004), and the illuminating probe function (Thibault et al., 2009). The phase part of each reconstructed sample image was corrected for an offset and linear term, aligned, and combined in a CT reconstruction as described by Guizar-Sicairos et al. (2011). Alignment in the horizontal x-direction, perpendicular to the axis of sample rotation, was refined based on tomographic consistency as described by Guizar-Sicairos et al. (2015). Based on line profiles extracted across sharp edges in the tomograms, *e.g.*, at the boundary between bone and air, we estimate the 3D spatial resolution of the results to be between 100 and 150 nm. We note that the resolution in these results is limited by angular sampling. The PXCT resolution d_{res} could be improved to the order of the voxel size, $d_{voxel} \leq d_{res} < (\pi/2) \times FOV_x / N_{proj}$, by increasing the number of projections N_{proj}.

2.6. Image processing

A PXCT image of the LCN structure comprises a 3D network of voids within a matrix. As a consequence, the histogram of values in our image shows two peaks. The gray levels in the histogram correspond quantitatively to electron density values, which can be converted to mass density as a function of an assumed chemical composition (Diaz et al., 2012). We approximate the bone matrix as pure hydroxyapatite. The density distribution for bone is somewhat skewed by partial-volume effects, created by averaging at the borders of the intricate structure of the LCN, and irregular border of the sample. To allow us to segment the fine details of the LCN from the sample, we therefore use morphological segmentation according to the following procedure (Ciani et al., 2016). A preliminary gray-level thresholding together with fill and closing operations, masks the air background around the sample and selects only the bone mineral matrix and LCN for segmentation using Avizo 3D software (Avizo 3D Software|FEI Software, n.d.). Electron densities in the histogram corresponding to hydroxyapatite were selected to discriminate the matrix voxels from the voxels on the boundary of the sample or the LCN (Ciani et al., 2016). Segmentation of the LCN was performed using a hysteresis thresholding procedure. Lacunae and canaliculi were identified within the segmented LCN using opening, labeling and cleaning operations. Quantitative geometrical parameters, such as the lacunae dimensions, number of canaliculi, average canalicular diameter, were computed as described in the following sections.

2.7. Osteocyte lacuna morphology

Lacunae were extracted from the PXCT images using a morphological opening operation with 7 voxels diameter spherical kernel, followed by dilation by 5 voxels diameter. The volume of each lacuna (Lc.V) was computed by two methods:

1. The number of empty voxels excluding canaliculi, Lc.V_1, and
2. by a fitting procedure we have described previously (Thibault et al., 2008), Lc.V_2.

The first method yields a quantitative volume Lc.V_1 in both ellipsoidal and in anisotropic, highly non-ellipsoidal cases, but it fails to provide reasonable results for comparison when partial lacunae are imaged. The second method, on the other hand, is a least-squares optimization procedure used to approximate the lacuna with an ellipsoid, the most frequently used form in similar studies (Maurel et al., 2011; Rochefort et al., 2010; Hesse et al., 2014). Our optimization method allows us to obtain an approximate lacunar volume, Lc.V_2, even when partial (> 50%) lacunae are present in the scan volume; however, the volume can be overestimated for non-ellipsoidal lacunae. A further benefit is that we can characterize the lacuna anisotropy by comparing the axis lengths of the best-fit ellipsoid; the ratio of the major axis 1 and semi-minor axis 2 is the degree of anisotropy, Lc.An_{12}, and similarly axis 1 compared to axis 3 gives Lc.An_{13}. The optimized fit residual, Lc.F_{opt} is the root-mean-square (rms) difference between the best-fit ellipsoid and the lacuna surface (Ciani et al., 2016), which gives a measure of the surface irregularity of the lacuna.

2.8. The lacuno-canalicular network

The canaliculi were characterized by an overall 'microporosity' in the matrix, Ca.V/MV, which we define distinctly from the bulk bone porosity, Po.V/TV, used in bone fragility studies (Chappard et al., 2013). The canalicular volume Ca.V was measured by integrating the number of voxels in the matrix which did not contain bone, excluding the lacuna. The microporosity expresses Ca.V as a fraction of the matrix tissue volume MV = TV − Lc.V_1, where TV is the total tissue volume and Lc.V_1 is the sum of voxels in the lacuna defined above. A so-called centerline tree skeletonization (Avizo 3D Software|FEI Software, n.d.), yielding an undirected graph description with tree topology and without loops, was performed on the segmented LCN to compute the average canalicular diameter Ca.Dm. The LCN was also analyzed in the vicinity of the lacuna using a distance map together with skeletonization (Avizo 3D Software|FEI Software, n.d.). Ca.Pr was the number of primary canaliculi, referring to those originating from the lacuna. Ca.Nb was the areal density of canaliculi as a function of surface area of the fitted ellipsoid. This quantity allows us to compare the LCN connectivity of full lacunae with that of partially imaged lacunae. Ca.Db was the length of the first dendritic branching distance.

2.9. Statistical analysis

Quantitative results were expressed as mean values among samples from the same group, with error bars of one standard deviation. Statistical analysis was performed using the Orange Data Mining (Demšar et al., 2013) Python library, Excel STATS and Statview. For all parameters, the normality of the distribution was tested with the Shapiro-Wilk test and the homogeneity of variance was tested with the Fisher F test. When the distribution of the data for each group respected the normality law and the variance of groups was homogeneous, parametric Student t-test for measures was used. When the distribution of at least one of the groups did not follow the normality law, comparisons between SHAM and GIO groups were performed with the non-parametric U Mann & Whitney test. The critical p-value for statistical significance in all cases was $p < 0.05$.

Table 2
microarchitecture of the trabecular and cortical bone (n = 14 SHAM, n = 15 GIO), evaluation of the % osteocyte lacunar occupancy after toluidine blue staining (n = 7 SHAM, n = 7 GIO).

Parameters	SHAM	GIO	p value
BV/TV (%)	17.9 ± 0.9	13.5 ± 0.8[a]	$p < 0.05$
Tb.Th (mm)	0.11 ± 0.002	0.09 ± 0.003[a]	$p < 0.05$
Ct.Ar (mm^2) Femur midshaft	8.3 ± 0.2	7.7 ± 0.2[a]	$p < 0.05$
Osteocyte lacunar occupancy (%)	53.7 ± 4.06	42.6 ± 3.8[a]	$p < 0.05$

[a] Indicates significance compared to the SHAM ($p < 0.05$).

3. Results

3.1. Glucocorticoid induced osteoporosis has deleterious effects on bone microarchitecture and histology

GIO provoked deleterious macroscopic consequences on femoral trabecular microarchitectural parameters (BV/TV, Tb.Th), and on cortical bone area at femur mid-diaphysis (Ct.Ar) (Table 2). Histology with toluidine blue staining on tibial cortical bone revealed that osteocyte lacunae area was not statistically different between both groups (mean value ± SD: SHAM 28.5 ± 2.3 *vs.* GIO 34.6 ± 3.6 μm^2). Osteocyte lacunae occupancy was significantly lower in the GIO group compared to the SHAM group (Table 2).

3.2. PXCT results

The results obtained to characterize the LCN in term of lacunae morphology and canalicular architecture are detailed in Table 3, summarizing the results for all morphological parameters for the SHAM and the GIO group. Fig. 3 presents the result of the segmentation of the bone tissue from its surroundings.

In Fig. 3(a) the whole sample volume of interest (VOI) is shown, and Fig. 3(b) shows the sample virtually bisected revealing an axial nano-CT image. In the nano-CT slice, the bone matrix is shown in grayscale, while the surrounding air, the lacunae sections and the parts of the LCN traversing this image slice are shown in black. In Fig. 3(c) a volume rendering of the segmented LCN in the bisected region reveals a detailed 3D view of the two lacunae and interconnecting canaliculi. The lacunae were measured to be around 200 μm^3 in volume, with the SHAM group being larger than GIO group on average ($p > 0.05$). Fig. 4 shows the fitting results for (a) entire and (b) partially imaged lacunae. A greater variation in volume was evident in the GIO group, which we attribute to the irregularity in the lacunar shape displayed in this group (see Fig. 5). This irregularity gives us less predictive power to assign an unknown lacuna to one of the sample groups based on volume alone ($p > 0.05$). However, quantifying the departure of the lacuna shape from ellipsoidal is informative.

Table 3
Mean and standard deviation for the morphological parameters of SHAM and GIO samples.

	SHAM	GIO	p
Number of donors	5	4	–
Number of samples	5	6	–
Total number of lacunae	6	15	–
$Lc.V_1$ [μm^3]	200 ± 40 (n = 5)	168 ± 79 (n = 12)	0.41
$Lc.V_2$ [μm^3]	213 ± 44 (n = 6)	170 ± 79 (n = 15)	0.23
$Lc.An_{12}$	0.49 ± 0.16 (n = 6)	0.61 ± 0.21 (n = 15)	0.19
$Lc.An_{13}$	0.199 ± 0.113 (n = 6)	0.289 ± 0.15 (n = 15)	0.102
$Lc.F_{opt}$ [μm]	0.41 ± 0.10 (n = 6)	0.72 ± 0.27 (n = 15)	0.0064**
Ca.V/MV (microporosity)	0.025 ± 0.010 (n = 5)	0.020 ± 0.009 (n = 5)	0.45
Ca.Dm [nm]	165 ± 8 (n = 4)	152 ± 6.5 (n = 4)	0.053
Ca.Nb [μm^{-2}]	0.36 ± 0.09 (n = 6)	0.24 ± 0.07 (n = 12)	0.0106*
Ca.Pr	near to 80 (n = 6)	near to 80 (n = 15)	> 0.05
Ca.Db [μm]	near to 1.1 (n = 6)	near to 1.1 (n = 15)	> 0.05

Lc = lacuna; Ca = canaliculi; TV = tissue volume; V_1, V_2 = lacuna volumes computed by methods 1 and 2 described in Materials and Methods; An_{12}, An_{13} = degrees of anisotropy; Ca.Dm = canaliculi diameter, $Lc.F_{opt}$ = optimization function; Ca.V/MV = microporosity as the ratio of the volume occupied by canaliculi to the total matrix tissue volume; Ca.Nb = number of canaliculi originating from the lacuna per ellipsoidal surface unit; Ca.Pr = mean number of primary canaliculi directly connected to the lacuna; Ca.Db = length of the first dendritic branching distance. In the right column, the p value from the Wilcoxon-Mann-Whitney test is given, and significant differences are indicated (*, $p < 0.05$; **, $p < 0.01$).

The anisotropy parameters in Table 3 relate the proportionality of the best-fit ellipsoid axes. An increase in both $Lc.An_{12}$ and $Lc.An_{13}$ in the GIO group indicates less anisotropy in both directions, *i.e.*, the ellipsoid is more spherical for the GIO lacunae than for SHAM ($p > 0.05$).

The parameter Lc. $F_{opt} = \sqrt{\sum_i (\overline{AB}_i)^2/N}$ is the root-mean-square (rms) difference between the best-fit ellipsoid and the lacuna surface calculated from the distances $\overline{AB}$ over the N surface points as shown in Fig. 6 (Ciani et al., 2016). The calculated optimization residual $Lc.F_{opt}$ is significantly higher in the GIO group than in the SHAM group ($p = 0.0064$).

The quantity Ca.V/MV represents the microporosity as the ratio of the volume occupied by canaliculi to the total matrix tissue volume. The average microporosity in the GIO group was 20% lower than in the SHAM, however, due to inter-sample variations it is impossible to conclude that the difference in microporosity between the SHAM and GIO groups is significant ($p > 0.05$). Nevertheless, when inspecting the PXCT images of the GIO samples in detail we observed large areas of disruption of the LCN in two samples. Fig. 7(a) shows an area, indicated with a white arrow, where canaliculi are absent and lacunae remain isolated or only partially connected. The tomogram slice, Fig. 7(b), shows clearly that this region contains material with identical density to the bone matrix without contrasting features. Fig. 7(c) shows LCN disruption in a different sample from the GIO group. Fig. 8(a) shows a lacuna extracted from a SHAM sample as an example of the ellipsoidal shape and regular connections in all directions to the LCN, while Fig. 8(b) shows a view of the lacuna on the right side of the sample imaged in Fig. 7(a), bordering on the disrupted LCN region.

The primary canaliculi were characterized by the spatial density of primary canaliculi directly connected with the lacuna surface. A skeletonization modulus algorithm (see Fig. 9) was used to obtain a directed graph network structure from the segmented LCN, amenable to statistical analysis. The number of primary canaliculi, Ca.Pr, and the distance to the first dendritic branching point, Ca.Db, were found to be approximately the same in both sample groups ($p > 0.05$) indeed, there were one average around 80 connections to the LCN per lacuna and a distance of the order of 1.1 μm to the first bifurcation and between other LCN nodes. The overall mean canalicular diameter, Ca.Dm, was slightly statistically un-significantly smaller in G (152 ± 6.5) nm than in SHAM (165 ± 8) nm ($p = 0.053$), and the spatial density of LCN connections, Ca.Nb, significantly decreased from 0.36 μm^{-2} (SHAM) to 0.24 μm^{-2} (GIO) ($p = 0.0106$).

4. Discussion

The improvement of the osteocyte lacuna and LCN imaging microscopy methods is necessary to contribute to better understanding of the involvement of the LCN parameters on the control of bone remodeling and homeostasis regulated by the osteocyte, in different physio-pathological contexts.

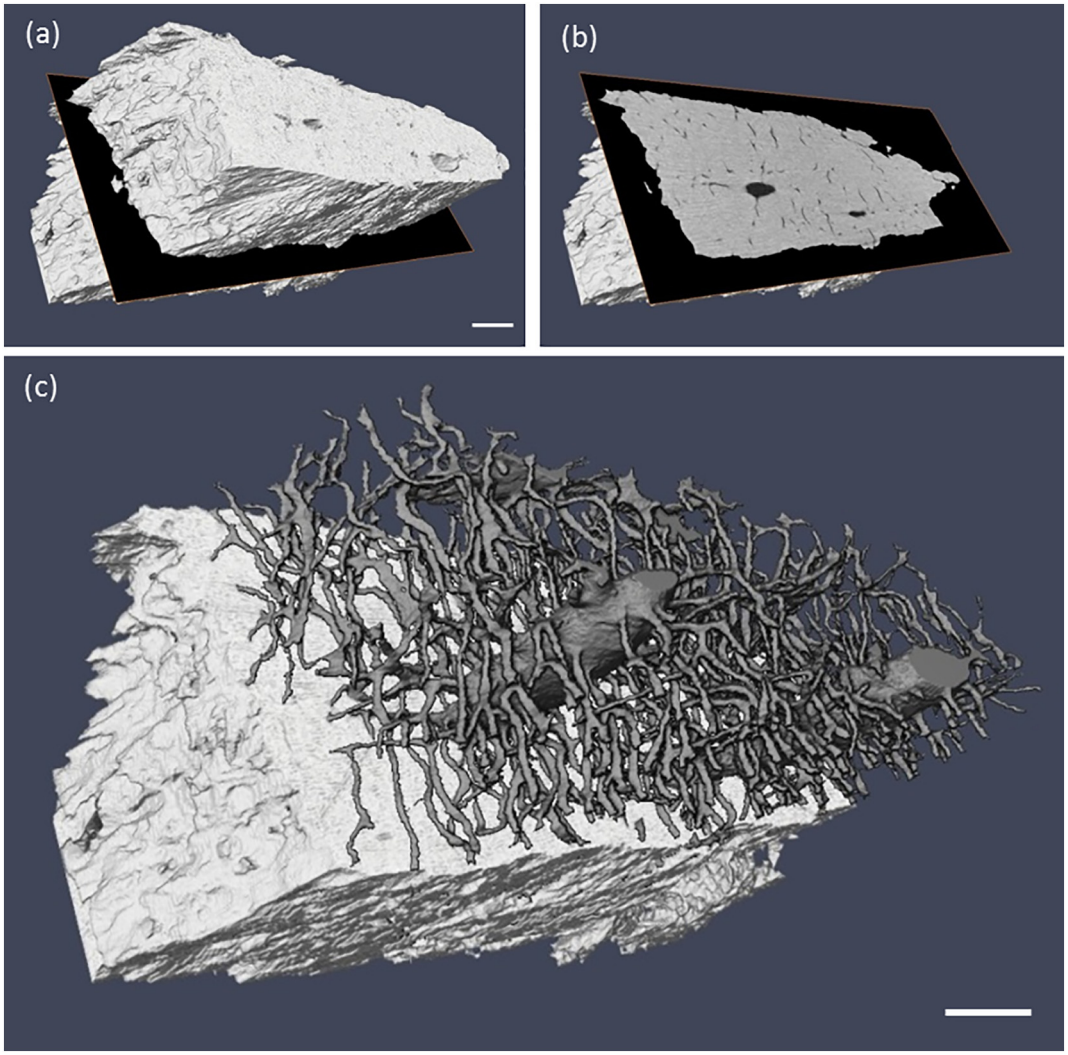

Fig. 3. (a) 3D rendering of the masked sample volume. A slice through the tomogram data set is indicated and shown in (b) where the LCN structure is visible as voids in black on the gray background of the matrix. (c) Rendering of the LCN structure above the tomogram slice in (b). The white scale bar in (a) and (c) represents a length of 10 μm.

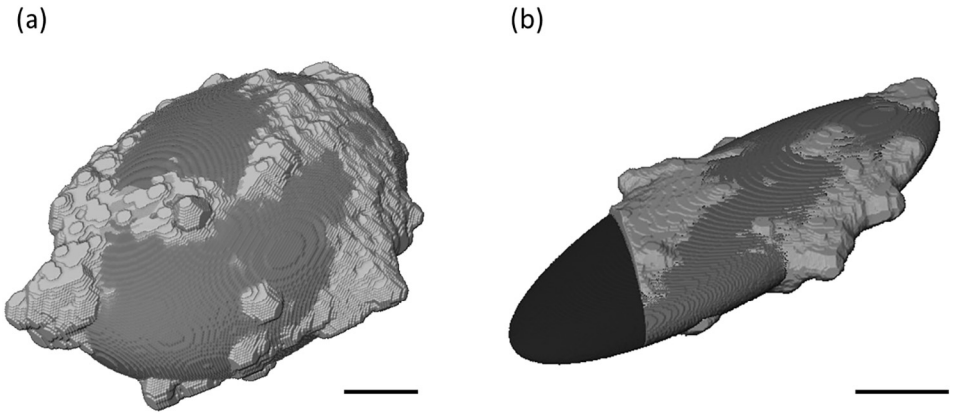

Fig. 4. Ellipsoidal fit for (a) an entire lacuna from a SHAM sample, and (b) a partial lacuna from a SHAM sample that was bisected by the edge of the reconstructed tomogram volume. The black volume in (b) shows the volume extension approximated by the fitted ellipsoid for the partially imaged lacuna. The black scale bar in each image represents 1 μm.

Previous literature devoted to such osteocyte characterization, has presented different conditions for bone samples preparation, such as resin casting, rhodamine labelling, inter alia (Pazzaglia and Congiu, 2013; Kerschnitzki et al., 2013; Repp et al., 2017), and different imaging methods such as scanning and transmission electron microscopy (SEM and TEM, respectively), combined serial focused ion beam/scanning electron microscopy (FIB-SEM), confocal microscopy, and X-rays tomography methods that yield detailed information on LCN, such as network architecture, density and connectivity (Schneider et al., 2011; Kerschnitzki et al., 2013; Karunaratne et al., 2016). Classic SEM and TEM remain 2D imaging methods, and can involve complex sample preparation. FIB-SEM is a 3D method affording a quantitative 3D assessment of the LCN at a resolution on the order of a few tens of nm, but it is time consuming, requires complicated sample preparation, and the

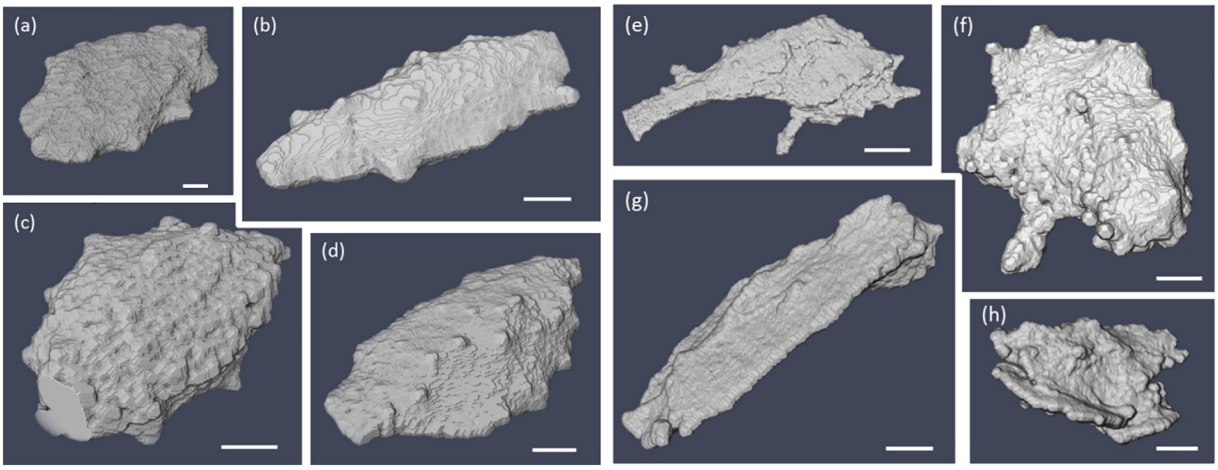

Fig. 5. (a–d) Examples of lacunae extracted from SHAM samples showing regular ellipsoidal-like shapes, and (e–h) from GIO samples, showing irregularly shaped lacunae. The scale bar in each image represents 1 μm.

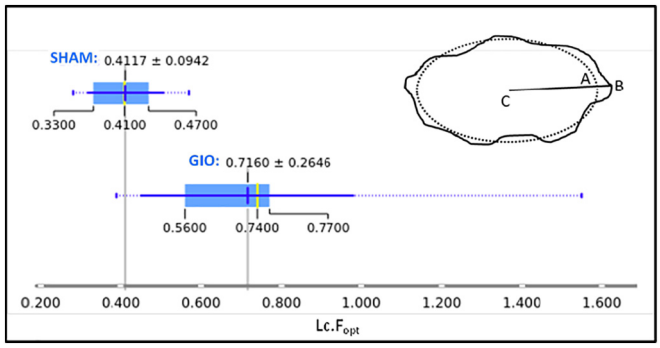

Fig. 6. A box-and-whisker plot summarizes the optimization residual $Lc.F_{opt}$ values for each group, indicating the wide variation in the GIO group compared to the SHAM group, and the significant difference in their distributions. The mean value and standard deviation is indicated above each boxplot. The dotted lines extend to the outliers beyond 1.5 times the interquartile range from the mean. The Wilcoxon-Mann-Whitney test yields $p = 0.0046$ for these two distributions. INSET: An illustration of the ellipsoidal fitting: the dotted line represents a section of the fitted ellipsoid; the solid line represents the lacuna surface. The departure from ellipsoidal is quantified by Lc. $F_{opt} = \sqrt{\sum_i (\overline{AB}_i)^2/N}$ where $\overline{AB}$ is the distance between the best-fit ellipsoid at A and the surface voxel B in the direction toward the center C, and N is the total number of surface points.

spatial resolution is not isotropic in 3D (Schneider et al., 2011). Confocal microscopy does not have sufficient spatial resolution (near to the range 200–280 nm) to reveal details of lacunar shape, but provides much larger field of view and very accurate data on network density and connectivity (Kerschnitzki et al., 2013; Repp et al., 2017).

PXCT constitutes a lensless imaging technique, which involves recording a sequence of X-ray diffraction patterns from a sample, exploiting the high phase sensitivity to produce quantitative and absolute 3D electron density maps. PXCT method presents the advantage to provide an absolute sub-micron mineral density quantification (Dierolf et al., 2010). The very high spatial resolution, demonstrated to 16 nm to date (Holler et al., 2014), provided by PXCT imaging gives us the possibility to study the fine structure of the cortical bone and its 3D microarchitecture in the vicinity of the osteocyte lacuna. The crucial involvement of the osteocyte in bone remodeling, and the role of this cell in some osteo-articular pathologies, has been the focus of several publications in the last decade (Bonewald, 2011; Achiou et al., 2015; Maurel et al., 2011; Rochefort et al., 2010), stimulating a strong interest in obtaining detailed knowledge on the osteocyte's biology. Among the different biological characteristics of the osteocyte, the morphology of the osteocyte lacuna and its LCN could provide a key etiological biomarker for pathologies such as osteoarthritis, osteopetrosis, osteonecrosis, or osteoporosis (van Hove et al., 2009; Hesse et al., 2014).

From previous studies (Jia et al., 2006; Rochefort et al., 2010; Hesse et al., 2014), it is known that GC treatment causes a decrease in osteocyte lacunar occupancy and an increase in osteocyte apoptosis in the cortical bone (Jia et al., 2006). Moreover, it has been shown that GC administration affects vascularity and solute transport in the LCN (Weinstein et al., 2010; Knothe Tate et al., 2004). Our study provides the opportunity to study GC effects at a high 3D resolution (about 100–150 nm) and to compare the LCN in healthy and GC-induced osteoporotic samples in terms of osteocyte lacuna and canaliculi morphology.

The osteocyte lacunar volumes obtained for the SHAM group in our study are concordant with previously published values (Schneider et al., 2010; Britz et al., 2012; Bach-Gansmo et al., 2015). The lacunae studied from our GIO group samples are smaller, but with a larger inter-sample dispersion of values than SHAM, whether their volumes were obtained by counting voxels ($Lc.V_1$) or assuming that the lacunae can be approximated by a fitted ellipsoid ($Lc.V_2$). We cannot conclude from these results that this is a significant difference. Indeed, in our previous results we have evaluated the osteocyte lacunae cross-sectional area in GIO and SHAM groups without observing significant differences (Achiou et al., 2015). Mean lacuna area has been previously reported to increase in GC models in mice at the trabecular part in vertebrae sections (Lane et al., 2006). More recently, Karunaratne et al. have measured the osteocyte lacunae volume compared to tissue volume (osteocyte lacunae density) at the tibiae shaft in a mice model of steroid-induced osteoporosis, by synchrotron X-ray micro-computed tomography at a spatial resolution of 3.2 μm (Karunaratne et al., 2016). Their results indicated a significant reduction in lacunae density ($p < 0.001$). This recent result from literature strengthens our $Lc.V_1$–$Lc.V_2$ results in the GIO group.

The degrees of anisotropy $Lc.An_{12}$ and $Lc.An_{13}$ are lower, but not significantly, in the SHAM group, resulting in a lower sphericity of the best-fit ellipsoid compared to the results for the GIO group lacunae. However, fitting an ellipsoid to the GIO group lacuna faces potential difficulties, since these lacunae are far more irregular and non-ellipsoidal in shape (shown in Fig. 5). We quantified this by comparing the rms departure from the best-fit ellipsoid, $Lc.F_{opt}$, which was far larger for the GIO group than SHAM (Fig. 6). Irregularity in lacunar morphology has been reported in other osteoarticular diseases such as osteoarthritis (Jaiprakash et al., 2012) and alcohol-induced osteoporosis (Maurel et al., 2011). The ability to see inside the lacunar volume in 3D within the PXCT images reveals that, in some samples, some lacunae

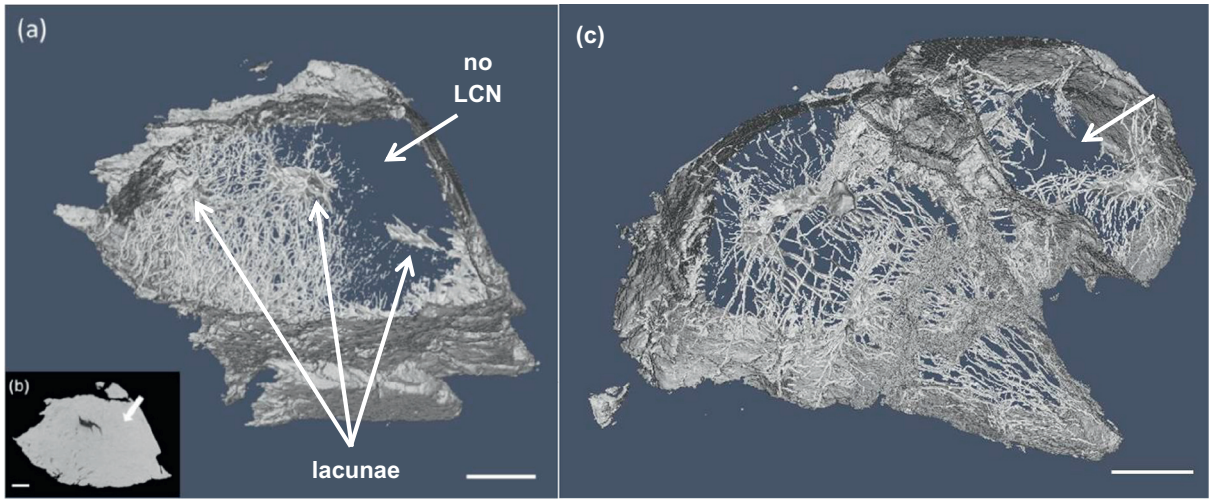

Fig. 7. (a) An image of the segmented LCN showing, indicated by a white arrow, approx. (10 × 20 × 40) μm^3 region with absent canaliculi, surrounded by isolated, disconnected lacunae, in an example from the GIO group; (b) a tomogram slice in this region confirms the absence of canaliculi, with a featureless matrix region highlighted by a white arrow; (c) shows another GIO group sample with a region containing no canaliculi. The white scale bar in each image represents 10 μm.

are partially filled with material that has the same density as the bone matrix which surrounds the lacuna and LCN.

Fig. 10 shows a PXCT cross-section of an osteocyte lacuna which has dense material inside. For consistency in the analysis we did not include these lacunae in the volumetric comparisons between GIO and SHAM, since we assume that in these regions the osteocyte had undergone apoptosis and some bone remineralization had taken place.

The microporosity, Ca.V/MV, was defined as the number of voxels belonging to canaliculi as a fraction of the bone matrix voxels. The lacuna volume was excluded from this analysis to isolate any differences between SHAM and GIO groups based on changes in the canalicular network. This definition allows us to analyze the differences between healthy bone and GIO bone without including blood vessels, Haversian canals, trabecular bone, or osteocyte lacunae, which are typically included in BMD and bone porosity measurements. It was found that the microporosity for the GIO group was decreased in comparison to SHAM, indicating that the canaliculi are either less numerous, or they are thinner in average diameter when GC treatment has been administered. Our microporosity quantification does not reveal a significant difference between these groups. However, for GIO samples in two obvious cases (Fig. 7), large regions were discovered having no canaliculi, containing only a featureless bulk of dense matrix material. This type of disruption of the otherwise intricately detailed and uniformly distributed LCN was only observed in samples from the GIO group and was not seen in any SHAM samples. A significant effect of GC on the LCN was obtained when analyzing the number density, Ca.Nb, of primary canaliculi connecting the LCN to the lacuna per unit surface area. Although the number of primary canaliculi, Ca.Pr ≈ 80 for both SHAM and GIO, the spatial density of connections was significantly lower in GIO. We conclude from Figs. 7, 8(b) and 10 that lacunae in samples of the GIO group are likely to be markedly non-ellipsoidal due to changes induced by GC treatment, and we suggest that there are remodeling events which occur to occlude existing lacunae and disrupt the LCN.

4.1. Limitations of this study

Our conclusions must be considered in parallel with the limitations of this study. The extended X-ray scanning times for PXCT had as consequence that a limited number of samples were able to be scanned in a feasible amount of experiment time at a large national research infrastructure such as the Swiss Light Source. In total, we have reported results from PXCT scans of five control samples containing six analyzed lacunae, and six glucocorticoid-treated samples containing fifteen lacunae. The measurements at room temperature do not permit measurement of the organic cellular components which prevented an analysis of the cellular effects of GC treatment; this limitation can be alleviated by measurements under cryogenic protection (Howells et al., 2009; Shahmoradian et al., 2017). Here, we confirmed that bone structure is radiation hard at this level of dose, and is not likely to be a

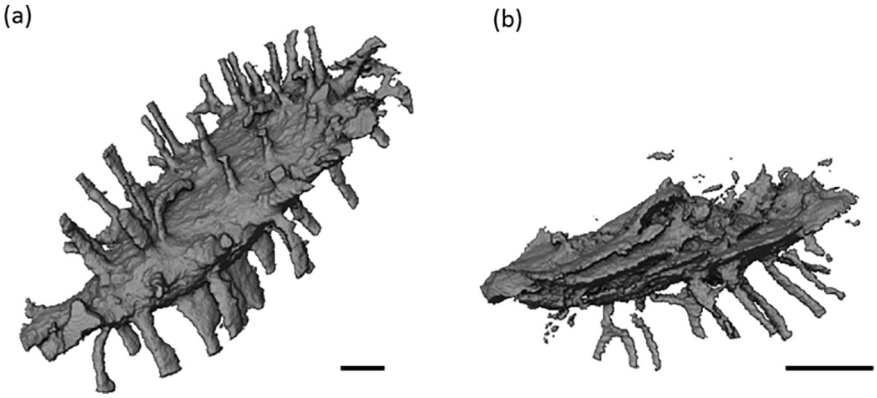

Fig. 8. Lacuna and primary canaliculi directly connected to it in the case of (a) a lacuna in SHAM group, and (b) a partially connected lacuna from the GIO group, from a location bordering on a disrupted LCN region. The black scale bar in each image represents 1 μm.

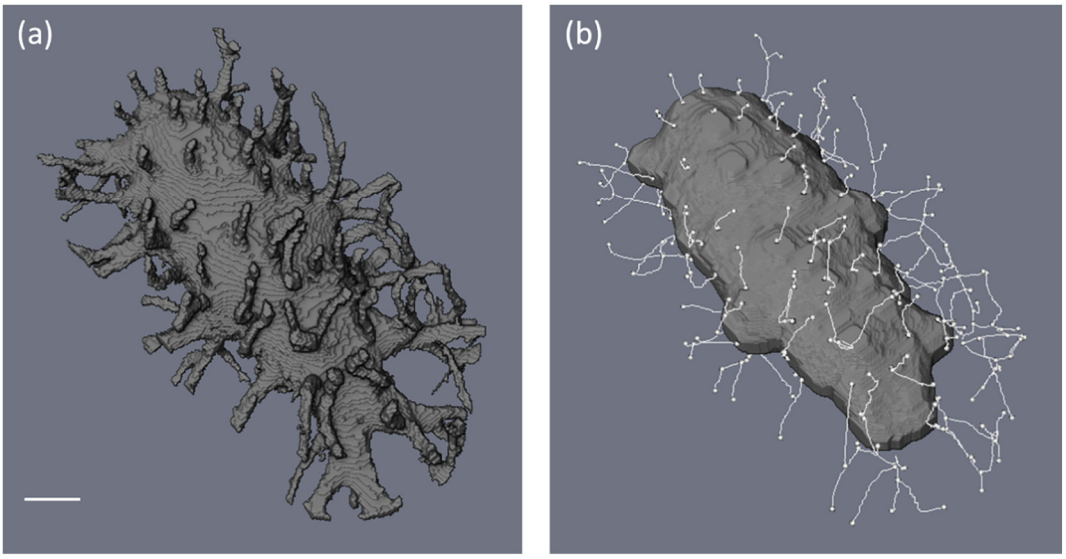

Fig. 9. (a) Ellipsoidal volume of interest extracted around the center of the lacuna, segmented to remove the bone matrix, (b) skeletonization of the LCN in the vicinity of the lacuna. This procedure yields the number of primary canaliculi directly connected to the lacuna, Ca.Pr, and the length of the first branching distance, Ca.Db. The white scale bar in (a) represents 1 μm.

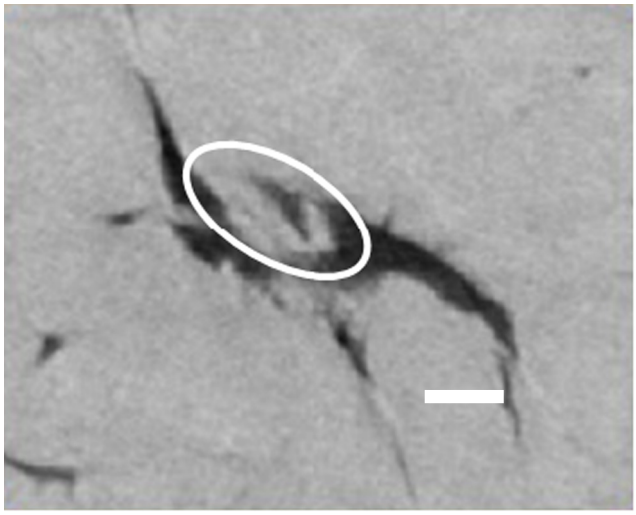

Fig. 10. Part of a tomogram slice through an osteocyte lacuna from the glucocorticoid-treated (GIO) group, showing gray matrix material both inside and outside the black lacuna. The material partially filling the lacuna (white oval) has the same density as the surrounding matrix. The white scale bar indicates 2 μm.

serious limitation for morphological studies of the LCN at the resolution presented in this study.

5. Conclusion

We have analyzed nano-CT images of samples extracted from cortical bone from the upper half of the rat tibial diaphysis, to non-destructively investigate the nanoscale effects of GC treatment on the osteocyte LCN. The nano-CT images quantify the density within the bone samples on a 40 nm voxel-grid, at a resolution of 100–150 nm. We have demonstrated that in this GIO animal model, the spatial density of primary canalicular connections Ca.Nb was significantly lower in the GC treated group than in controls. We have confirmed that the osteocyte lacunae are largely ellipsoidal in SHAM samples, whereas the lacunae become more spherical in overall shape and significantly irregular in form in the GC treated samples, when the latter is quantified by the rms departure from an ellipsoidal fitting. Severe disruption of the LCN was observed in GC treated samples, and we attribute this to a remineralization of these bone regions resulting in occluded lacunae, and lower microporosity than seen in control samples.

Transparency document

The Transparency document associated with this article can be found, in the online version.

Acknowledgements

The authors acknowledge Paul Scherrer Institut, Villigen, Switzerland for provision of synchrotron radiation beam time at the cSAXS beamline of the Swiss Light Source (SLS proposals 20110196, 20120152, 20150515). This work was financially supported by the Région Centre Val de Loire (Convention SOLEIL/Région Centre 201100070591, project “Caractérisation du tissu osseux aux échelles micro et nanométriques”). Esther H. R. Tsai is supported by the Swiss National Science Foundation (SNSF) grant number 200021_152554. We are particularly grateful to Dr. Jean-Pierre Samama and Dr. Claude-Laurent Benhamou who supported this project since the beginning. The authors acknowledge Dr. Delphine Benaitreau, Dr. Gäel Y. Rochefort and Mr. Masnsen Cherief for assistance with sample preparation, and participation in the imaging experiments at SLS. The authors further acknowledge Dr. Rachid Jennane for taking part in discussion of the results, and Dr. Zahra Achiou and Mr. Eric Dolleans for assistance with the animal experiments. We thank Dr. Andreas Menzel for his comments on the manuscript.

Authorship roles

Conceived the project: CMK, SP. Carried out synchrotron experiments: CMK, EHRT, AD, MGS, MH, SP, AC. Sample preparation: AC, SP, CMK. Data analysis: AC, CMK, AD. Data interpretation: AC, CMK, SP, HT, EL. Drafting manuscript: AC, CMK, SP, HT, EL. Approving final version of manuscript: all authors. CMK takes responsibility for the integrity of the data analysis.

References

Achiou, Z., Toumi, H., Touvier, J., Boudenot, A., Uzbekov, R., Ominsky, M.S., et al., 2015 Dec. Sclerostin antibody and interval treadmill training effects in a rodent model of glucocorticoid-induced osteopenia. Bone 81, 691–701.

FEI Visualization Sciences Group, Burlington MA, *Avizo Fire v. 9.0*

Bach-Gansmo, F.L., Weaver, J.C., Jensen, M.H., Leemreize, H., Mader, K.S., Stampanoni, M., et al., 2015 Jul. Osteocyte lacunar properties in rat cortical bone: differences between lamellar and central bone. J. Struct. Biol. 191 (1), 59–67.

Bonewald, L.F., 2011 Feb. The amazing osteocyte. J. Bone Miner. Res. 26 (2), 229–238.

Briot, K., Roux, C., 2015. Glucocorticoid-induced osteoporosis. RMD open 1 (1), e000014.

Britz, H.M., Carter, Y., Jokihaara, J., Leppänen, O.V., Järvinen, T.L.N., Belev, G., et al., 2012 Nov. Prolonged unloading in growing rats reduces cortical osteocyte lacunar density and volume in the distal tibia. Bone 51 (5), 913–919.

Canalis, E., Mazziotti, G., Giustina, A., Bilezikian, J.P., 2007. Glucocorticoid-induced osteoporosis: pathophysiology and therapy. Osteoporos. Int. 18 (10), 1319–1328.

Chappard, C., Bensalah, S., Olivier, C., Gouttenoire, P.J., Marchadier, A., Benhamou, C., et al., 2013. 3D characterization of pores in the cortical bone of human femur in the elderly at different locations as determined by synchrotron micro-computed tomography images. Osteoporos. Int. 24 (3), 1023–1033.

Ciani, A., Guizar-Sicairos, M., Diaz, A., Holler, M., Pallu, S., Achiou, Z., et al., 2016. Segmentation of nanotomographic cortical bone images for quantitative characterization of the osteoctyte lacuno-canalicular network. In: AIP Conference Proceedings, (p. 020040).

Currey, J.D., 1964. Three analogies to explain the mechanical properties of bone. Biorheology 2 (1).

Dallas, S.L., Veno, P.A., 2012. Live imaging of bone cell and organ cultures. Bone Res. Protoc. 425–457.

Demšar, J., Curk, T., Erjavec, A., Gorup, Č., Hočevar, T., Milutinovič, M., et al., 2013. Orange: data mining toolbox in Python. J. Mach. Learn. Res. 14 (1), 2349–2353.

Diaz, A., Trtik, P., Guizar-Sicairos, M., Menzel, A., Thibault, P., Bunk, O., 2012 Jan. Quantitative x-ray phase nanotomography. Phys. Rev. B 85 (2), 020104.

Dierolf, M., Menzel, A., Thibault, P., Schneider, P., Kewish, C.M., Wepf, R., et al., 2010. Ptychographic X-ray computed tomography at the nanoscale. Nature 467 (7314), 436–439.

Everts, V., Niehof, A., Tigchelaar-Gutter, W., Beertsen, W., 2012. Transmission electron microscopy of bone. Methods Mol. Biol. 816, 351–363.

Faulkner, H.M.L., Rodenburg, J.M., 2004 Jul. Movable aperture lensless transmission microscopy: a novel phase retrieval algorithm. Phys. Rev. Lett. 93 (2), 023903.

Frenkel, B., White, W., Tuckermann, J., 2015. Glucocorticoid-induced osteoporosis. In: Wang, J.C., Harris, C. (Eds.), Advances in Experimental Medicine and Biology, pp. 179.

Fritton, S.P., Weinbaum, S., 2009 Jan. Fluid and solute transport in bone: flow-induced mechanotransduction. Annu. Rev. Fluid Mech. 41, 347–374.

Frost, H.M., 1960 Jan. In vivo osteocyte death. J. Bone Joint Surg. Am. 42 (A), 138–143.

Guizar-Sicairos, M., Diaz, A., Holler, M., Lucas, M.S., Menzel, A., Wepf, R.A., et al., 2011 Oct. Phase tomography from x-ray coherent diffractive imaging projections. Opt. Express 19 (22), 21345.

Guizar-Sicairos, M., Boon, J.J., Mader, K., Diaz, A., Menzel, A., Bunk, O., 2015 Mar. Quantitative interior x-ray nanotomography by a hybrid imaging technique. Optica 2 (3), 259.

Henkel, J., Woodruff, M.A., Epari, D.R., Steck, R., Glatt, V., Dickinson, I.C., et al., 2013. Bone regeneration based on tissue engineering conceptions — a 21st century perspective. Bone Res. 1 (3), 216–248.

Hesse, B., Langer, M., Varga, P., Pacureanu, A., Dong, P., Schrof, S., et al., 2014 Feb. Alterations of mass density and 3D osteocyte lacunar properties in bisphosphonate-related osteonecrotic human jaw bone, a synchrotron μCT study. PLoS One 9 (2), e88481.

Holler, M., Raabe, J., 2015. Error motion compensating tracking interferometer for the position measurement of objects with rotational degree of freedom. Opt. Eng. 54 (5), 54101.

Holler, M., Raabe, J., Diaz, A., Guizar-Sicairos, M., Quitmann, C., Menzel, A., et al., 2012 Jul. An instrument for 3D x-ray nano-imaging. Rev. Sci. Instrum. 83 (7), 073703.

Holler, M., Diaz, A., Guizar-Sicairos, M., Karvinen, P., Färm, E., Härkönen, E., et al., 2014. X-ray ptychographic computed tomography at 16 nm isotropic 3D resolution. Sci. Rep. 4, 3857.

van Hove, R.P., Nolte, P.A., Vatsa, A., Semeins, C.M., Salmon, P.L., Smit, T.H., et al., 2009 Aug. Osteocyte morphology in human tibiae of different bone pathologies with different bone mineral density–is there a role for mechanosensing? Bone 45 (2), 321–329.

Howells, M.R., Beetz, T., Chapman, H.N., Cui, C., Holton, J.M., Jacobsen, C.J., et al., 2009 Mar. An assessment of the resolution limitation due to radiation-damage in X-ray diffraction microscopy. J. Electron Spectrosc. Relat. Phenom. 170 (1–3), 4–12.

Jaiprakash, A., Prasadam, I., Feng, J.Q., Liu, Y., Crawford, R., Xiao, Y., 2012. Phenotypic characterization of osteoarthritic osteocytes from the sclerotic zones: a possible pathological role in subchondral bone sclerosis. Int. J. Biol. Sci. 8 (3), 406–417.

Jia, D., O'Brien, C.A., Stewart, S.A., Manolagas, S.C., Weinstein, R.S., 2006 Dec. Glucocorticoids act directly on osteoclasts to increase their life span and reduce bone density. Endocrinology 147 (12), 5592–5599.

Johnson, I., Bergamaschi, A., Buitenhuis, J., Dinapoli, R., Greiffenberg, D., Henrich, B., et al., 2012 Nov. Capturing dynamics with Eiger, a fast-framing X-ray detector. J. Synchrotron Radiat. 19 (6), 1001–1005.

Jones, C.W., Smolinski, D., Keogh, A., Kirk, T.B., Zheng, M.H., 2005. Confocal laser scanning microscopy in orthopaedic research. Prog. Histochem. Cytochem. 40 (1), 1–71.

Kanis, J.A., Johansson, H., Oden, A., Johnell, O., de Laet, C., Melton III, L.J., et al., 2004 Jun. A meta-analysis of prior corticosteroid use and fracture risk. J. Bone Miner. Res. Off. J. Am. Soc. Bone Miner. Res. 19 (6), 893–899.

Karunaratne, A., Xi, L., Bentley, L., Sykes, D., Boyde, A., Esapa, C.T., et al., 2016 Mar 5. Multiscale alterations in bone matrix quality increased fragility in steroid induced osteoporosis. Bone 84, 15–24.

Kerschnitzki, M., Kollmannsberger, P., Burghammer, M., Duda, G.N., Weinkamer, R., Wagermaier, W., et al., 2013 Mar 13. Architecture of the osteocyte network correlates with bone material quality. J. Bone Miner. Res. 28 (8), 1837–1845.

Knothe Tate, M.L., Adamson, J.R., Tami, A.E., Bauer, T.W., 2004 Jan. The osteocyte. Int. J. Biochem. Cell Biol. 36 (1), 1–8.

Kraft, P., Bergamaschi, A., Broennimann, C., Dinapoli, R., Eikenberry, E.F., Henrich, B., et al., 2009 May. Performance of single-photon-counting PILATUS detector modules. J. Synchrotron Radiat. 16 (3), 368–375.

Lane, N.E., Yao, W., Balooch, M., Nalla, R.K., Balooch, G., Habelitz, S., et al., 2006 Mar. Glucocorticoid-treated mice have localized changes in trabecular bone material properties and osteocyte lacunar size that are not observed in placebo-treated or estrogen-deficient mice. J. Bone Miner. Res. Off. J. Am. Soc. Bone Miner. Res. 21 (3), 466–476.

Langer, M., Peyrin, F., 2016 Feb. 3D X-ray ultra-microscopy of bone tissue. Osteoporos. Int. 27 (2), 441–455.

Langer, M., Pacureanu, A., Suhonen, H., Grimal, Q., Cloetens, P., Peyrin, F., 2012. X-ray phase nanotomography resolves the 3D human bone ultrastructure. PLoS One 7 (8), e35691.

Maurel, D.B., Jaffre, C., Rochefort, G.Y., Aveline, P.C., Boisseau, N., Uzbekov, R., et al., 2011 Sep. Low bone accrual is associated with osteocyte apoptosis in alcohol-induced osteopenia. Bone 49 (3), 543–552.

O'Brien, C.A., Jia, D., Plotkin, L.I., Bellido, T., Powers, C.C., Stewart, S.A., et al., 2004 Apr. Glucocorticoids act directly on osteoblasts and osteocytes to induce their apoptosis and reduce bone formation and strength. Endocrinology 145 (4), 1835–1841.

Ohnaka, K., Taniguchi, H., Kawate, H., Nawata, H., Takayanagi, R., 2004. Glucocorticoid enhances the expression of dickkopf-1 in human osteoblasts: novel mechanism of glucocorticoid-induced osteoporosis. Biochem. Biophys. Res. Commun. 318 (1), 259–264.

Pazzaglia, U.E., Congiu, T., 2013 Feb 22. The cast imaging of the osteon lacunar-canalicular system and the implications with functional models of intracanalicular flow. J. Anat. 222 (2), 193–202.

Repp, F., Kollmannsberger, P., Roschger, A., Kerschnitzki, M., Berzlanovich, A., Gruber, G.M., et al., 2017. Spatial heterogeneity in the canalicular density of the osteocyte network in human osteons. Bone Rep. 6, 101–108.

Rochefort, G.Y., Pallu, S., Benhamou, C.L., 2010 Sep. Osteocyte: the unrecognized side of bone tissue. Osteoporos. Int. 21 (9), 1457–1469.

Rubin, M.A., Jasiuk, I., Taylor, J., Rubin, J., Ganey, T., Apkarian, R.P., 2003 Sep. TEM analysis of the nanostructure of normal and osteoporotic human trabecular bone. Bone 33 (3), 270–282.

Sambrook, P., Hughes, D., Nelson, A., Robinson, B., Mason, R., 2003 Dec. Osteocyte viability with glucocorticoid treatment: relation to histomorphometry. Ann. Rheum. Dis. 62 (12), 1215–1217.

Schneider, P., Meier, M., Wepf, R., Müller, R., 2010 Nov. Towards quantitative 3D imaging of the osteocyte lacuno-canalicular network. Bone 47 (5), 848–858.

Schneider, P., Meier, M., Wepf, R., Müller, R., 2011 Aug. Serial FIB/SEM imaging for quantitative 3D assessment of the osteocyte lacuno-canalicular network. Bone 49 (2), 304–311.

Schneider, C.A., Rasband, W.S., Eliceiri, K.W., 2012. NIH Image to ImageJ: 25 years of image analysis. Nat. Methods 9 (7), 671.

Schroer, C.G., Meyer, J., Kuhlmann, M., Benner, B., Günzler, T.F., Lengeler, B., et al., 2002 Aug. Nanotomography based on hard x-ray microscopy with refractive lenses. Appl. Phys. Lett. 81 (8), 1527–1529.

Shahmoradian, S.H., Tsai, E.H.R., Diaz, A., Guizar-Sicairos, M., Raabe, J., Spycher, L., et al., 2017. Three-dimensional imaging of biological tissue by cryo x-ray ptychography. Sci. Rep. 7 (1), 6291.

van Staa, T.P., 2006 Sep. The pathogenesis, epidemiology and management of glucocorticoid-induced osteoporosis. Calcif. Tissue Int. 79 (3), 129–137.

Thibault, P., Guizar-Sicairos, M., 2012. Maximum-likelihood refinement for coherent diffractive imaging. New J. Phys. 14 (6), 63004.

Thibault, P., Dierolf, M., Menzel, A., Bunk, O., David, C., Pfeiffer, F., 2008 Jul. High-resolution scanning X-ray diffraction microscopy. Science 321 (5887), 379–382.

Thibault, P., Dierolf, M., Bunk, O., Menzel, A., Pfeiffer, F., 2009 Mar. Probe retrieval in ptychographic coherent diffractive imaging. Ultramicroscopy 109 (4), 338–343.

Van Staa, T.P., Leufkens, H.G.M., Cooper, C., 2002. The epidemiology of corticosteroid-induced osteoporosis: a meta-analysis. Osteoporos. Int. 13 (10), 777–787.

Van Staa, T.P., Laan, R.F., Barton, I.P., Cohen, S., Reid, D.M., Cooper, C., 2003 Nov. Bone density threshold and other predictors of vertebral fracture in patients receiving oral glucocorticoid therapy. Arthritis Rheum. 48 (11), 3224–3229.

Van Staa, T.P., Leufkens, H.G.M., Abenhaim, L., Zhang, B., Cooper, C., 2005. Use of oral corticosteroids and risk of fractures. J. Bone Miner. Res. 20 (8), 1486–1493.

Weinstein, R.S., 2000 Apr. True strength. J. Bone Miner. Res. 15 (4), 621–625.

Weinstein, R.S., 2010 Mar. Glucocorticoids, osteocytes, and skeletal fragility: the role of bone vascularity. Bone 46 (3), 564–570.

Weinstein, R.S., 2011 Jul. Glucocorticoid-induced bone disease. N. Engl. J. Med. 365 (1), 62–70.

Weinstein, R.S., Jilka, R.L., Parfitt, A.M., Manolagas, S.C., 1998 Jul. Inhibition of osteoblastogenesis and promotion of apoptosis of osteoblasts and osteocytes by glucocorticoids. Potential mechanisms of their deleterious effects on bone. J. Clin. Invest. 102 (2), 274–282.

Weinstein, R.S., Chen, J.-R., Powers, C.C., Stewart, S.A., Landes, R.D., Bellido, T., et al., 2002 Apr. Promotion of osteoclast survival and antagonism of bisphosphonate-induced osteoclast apoptosis by glucocorticoids. J. Clin. Invest. 109 (8), 1041–1048.

Weinstein, R.S., Wan, C., Liu, Q., Wang, Y., Almeida, M., O'Brien, C.A., et al., 2010 Apr. Endogenous glucocorticoids decrease skeletal angiogenesis, vascularity, hydration, and strength in aged mice. Aging Cell 9 (2), 147–161.

You, L.-D., Weinbaum, S., Cowin, S.C., Schaffler, M.B., 2004 Jun. Ultrastructure of the osteocyte process and its pericellular matrix. Anat Rec A Discov Mol Cell Evol Biol 278 (2), 505–513.